ACS APPLIED MATERIALS & INTERFACES

Research Article

www.acsami.org

Covalently Coupled Ultrafine H-TiO_2 Nanocrystals/Nitrogen-Doped Graphene Hybrid Materials for High-Performance Supercapacitor

Shuhua Yang, Yuan Lin, Xuefeng Song,* Peng Zhang, and Lian Gao*

State Key Laboratory for Metallic Matrix Composite Materials, School of Materials Science and Engineering, Shanghai Jiao Tong University, Shanghai 200240, China

Supporting Information

ABSTRACT: Hydrogenated TiO_2 (H-TiO_2) are considered one of the most promising materials for supercapacitors given its low-cost, high conductivity, and enhanced electrochemical activity. However, the electrochemical performances of H-TiO_2 due to lacking suitable structures is unsatisfactory, and thus how to design energetic H-TiO_2-based electrode architectures still remains a great challenge. Herein, covalently coupled ultrafine H-TiO_2 nanocrystals/nitrogen-doped graphene (H-TiO_2/NG) hybrid materials were developed through a simple hydrothermal route followed by hydrogenation. Within this architecture, the strong interaction between H-TiO_2 nanocrystals and NG sheets via covalent chemical bonding affords high structural stability inhibiting the aggregation of H-TiO_2 nanocrystals. Meanwhile, the NG matrices function as an electrical highway and a mechanical backbone so that most of well-dispersed ultrafine H-TiO_2 nanocrystals are electrochemically active but stable. As a result, the optimized H-TiO_2/NG (H-TiO_2/NG-B) exhibited high reversible specific capacity of 385.2 F g^{-1} at 1 A g^{-1}, enhanced rate performance of 320.1 F g^{-1} at a high current density of 10 A g^{-1}, and excellent cycling stability with 98.8% capacity retention.

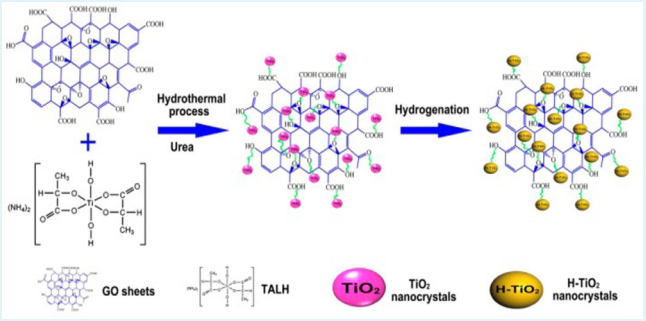

KEYWORDS: *nitrogen-doped graphene, ultrafine TiO_2 nanocrystals, hydrogenation, covalent chemical bond, high capacity, supercapacitor*

INTRODUCTION

Supercapacitors (SCs) are considered to be a promising green energy storage technology filling the gap between a battery and a traditional capacitor on the basis of both energy and power densities. Based on charge storage mechanisms, supercapacitors store charge by either rapid adsorption/desorption at the electrode surfaces (electric double layer capacitors) or Faradaic reactions on electrode materials (pseudocapacitors). Typically, pseudocapacitors based on transition metal oxides, hydroxides, and conducting polymers usually show higher capacitance through surface redox reactions than electric double layer capacitors (EDLCs) using carbon-based materials.[1−5]

Among various pseudocapacitance materials, TiO_2 has received special interest for supercapacitors because of their low cost, excellent chemical stability, abundance in nature, and minimum environmental impact.[6,7] However, the semiconducting nature of TiO_2 limits the electrical conductivity and impedes fast electron transport toward high rate capability and thus shows poor electrochemical stability and low rate capability. For this problem, a mount of efforts have been focused on developing three-dimensional (3D) architectures (for example, nanotube arrays) with sufficient open structures to overcome the low ion diffusion coefficient and provide a direct pathway for charge transport in TiO_2-based supercapacitors.[7−11] More recently, a substantial improvement of the capacitive performance for one-dimensional anodic titanium oxide (ATO) nanotube arrays was realized through hydrogenation, which is ascribed to the enhanced electrode conductivity and electrochemical activity associated with the effective hydrogen induced Ti^{3+} sites in TiO_2 lattices.[7,8,12,13] However, one-dimensional ATO nanotube arrays yield much lower volumetric density than nanopowders, and suffer from low production for practical applications. In addition, it is well-known that the Ti substrate is susceptible to hydrogen embrittlement, and thus the ATO nanotube arrays will be peeled off from the substrate during the H_2 annealing process. Moreover, fabricating TiO_2/carbon hybrids (e.g., TiO_2/carbon nanotube, TiO_2/graphene) also offers another way to improve the capacitance of supercapacitors due to the high specific surface area and good conductivity of carbon materials.[6,14−18] Although the electrochemical performances of those composites are improved by combining the merits of both components and mitigating the shortcomings of each component, those composites still suffer from low capacitances in the range of 100−200 F g^{-1} and poor rate capability under various aqueous and nonaqueous electrolytes.[6,14−17,19] There-

Received: May 20, 2015
Accepted: July 27, 2015
Published: July 27, 2015

DOI: 10.1021/acsami.5b04368
ACS Appl. Mater. Interfaces 2015, 7, 17884−17892

fore, to further push the TiO_2-based supercapacitors development, it is highly desirable to fundamentally improve the rate capability and capacitive behavior of electrodes through changing the intrinsic properties of both TiO_2 and carbon materials. Moreover, to the best of our knowledge, the exact interaction mechanism between TiO_2 and carbon materials remains poorly understood. This subject has been largely overlooked by the researchers. Graphene, which is composed of one atom thick sp^2 carbon network, is recently becoming one of the most promising matrices for metal oxides due to its unique properties, such as excellent electrical properties, high surface area over 2600 m^2 g^{-1}, and excellent mechanical flexibility. Particularly, chemically modified graphene (CMG) nanosheets in supercapacitors have shown great promise for industrial applications due to high accessible surface area, good electrical conductivity, enhanced electrochemical properties, and the low-cost raw material.[20−24] Inspired from our recent demonstration that nitrogen doping is one of the most effective methods to tailor the electronic properties of graphene-based materials and to improve the electrochemical performances for supercapacitors,[25,26] loading well-dispersed hydrogenated TiO_2 nanocrystals on nitrogen-doped graphene could address aforementioned limitations and thus improve the specific capacitance and stability of TiO_2 materials, as well as the rate capability.

Here, the hydrogenated TiO_2 nanocrystals/nitrogen-doped graphene (H-TiO_2/NG) hybrids were successfully synthesized via a two-step method for the first time. The interaction between H-TiO_2 nanocrystals and NG sheets was explored. Within such architecture, (1) the strong interaction between H-TiO_2 nanocrystals and NG sheets via covalent chemical bonding affords high structural stability inhibiting the aggregation of H-TiO_2 nanocrystals, which is key to both the excellent cycling stability and high rate capability; (2) the hydrogenation fundamentally modifies the electric conductivity and the electrochemical activity of TiO_2 nanocrystals by introducing oxygen vacancies (Ti^{3+} sites) in TiO_2 lattices; (3) the NG matrices function as an electronic highway and a mechanical backbone so that most of H-TiO_2 nanocrystals are electrochemically active but stable through the NG network; (4) the well-dispersed ultrafine TiO_2 nanocrystals (5−10 nm) on the NG sheets with little dead volume and large specific surface area are advantageous for the electrochemical utilization of TiO_2 active materials and offer a direct short pathway for electrolyte ions diffusion. To the best of our knowledge, the electrical conductivity and capacitive behavior of H-TiO_2/NG hybrids are fundamentally improved for supercapacitors through changing the intrinsic properties of both TiO_2 and graphene, which is significantly distinct from previously reported TiO_2-based hybrid nanostructures simply by changing the morphologies of TiO_2, the categories of carbon materials, or combination mode of the both components. Furthermore, these hybrids exhibit excellent electrochemical characteristics and high cycling stability and thus hold great potential as electrode materials for high-performance supercapacitors when compared to their counterparts.

EXPERIMENTAL SECTION

Synthesis of H-TiO_2/NG. Graphene oxide was synthesized from natural flake graphite (Alfa Aesar, 325 mesh, 99.8%) according to the modified Hummers method, which typically renders carbon concentrations of ∼65 wt % (wt %).[27] Then a certain amount of titanium bis (ammonium lactate) dihydroxide (TALH) aqueous solution (50%) and 20 mL of graphene oxide dispersion (2.5 mg mL^{-1}) were mixed with 0.1 g of urea. After being stirred for 15 min, the resulting solution was sealed into a 50 mL Teflon-lined stainless steel autoclave and heated at 160 °C for 24 h. After reaction, the autoclave was naturally cooled in air. The as-prepared products (TiO_2/NG hybrids) were separated by centrifugation, washed with distilled water and ethanol several times, and dried at 60 °C for 24 h. To prepare TiO_2 nanocrystals (or TiO_2/RGO hybrids), a similar procedure was performed except addition of GO (or urea). The RGO (or NG) was also prepared by the similar procedure without the addition of TALH and urea (or TALH). The H-TiO_2/NG hybrids, H-TiO_2/RGO hybrids, and H-TiO_2 nanocrystals were obtained by annealing the corresponding samples at 400 °C for 1 h in Ar/H_2 (5 wt % H_2) mixed atmosphere. Here, three kinds of H-TiO_2/NG hybrids with different ratios between H-TiO_2 and NG were synthesized. The contents of H-TiO_2 in the H-TiO_2/NG hybrids are 50.3, 88.7, and 92.5 wt % (evaluated from TGA); the corresponding samples are referred to as H-TiO_2/NG-A, H-TiO_2/NG-B, and H-TiO_2/NG-C, respectively. For the sample with optimum ratio of H-TiO_2 in hybrids, the corresponding counterparts are denoted as TiO_2/NG-B, H-TiO_2/RGO-B.

Material Characterization. X-ray diffraction (XRD) patterns of the samples were collected on a Goniometer Ultima IV (185 mm) diffractometer with Cu Kα radiation (λ = 1.5418 Å) at a step of 0.02° per second. The morphology and microstructure of the as-prepared products were examined by a JEOL JEM-2010F 200 kV transmission electron microscope. Fourier transform infrared (FTIR) spectra were taken with a Nicolet 6700 FTIR spectrometer. Raman spectra were carried out using a DXR Raman Microscope with an excitation length of 532 nm. X-ray photoelectron spectroscopy (XPS, Kratos AXIS Ultra DLD spectrometer) was used for determining the composition and chemical/oxidation state of the samples. A commercial CasaXPS 2.3.16 software package was used to process XPS spectra. In our case, the C 1s peak with a fixed value of 284.8 eV was used to calibrate all the binding energies for the prepared samples. For the narrow spectra, they were fitted by the combination of Gaussian and Lorentzian functions after removal of the Shirley backgrounds. Thermogravimetric analyses (TGA) and differential thermogravimetric (DTG) curves were run on a SDT Q600 V20.9 Build 20 thermogravimetric analyzer at a heating rate of 10 °C min^{-1} from 50 to 850 °C in air.

Electrochemical Measurements. The electrochemical properties of the samples were investigated under a three-electrode cell configuration in a 1 M KOH solution using a VMP3 multifunctional electrochemical analysis instrument (Bio-Logic, France). The working electrodes were fabricated by mixing 80 wt % active material, 15 wt % acetylene black, and 5 wt % polyvinylidene difluoride (PVDF) in *N*-methyl pyrrolidone (NMP) solvent. The resulting slurry was then loaded onto the nickel foam substrate (1 cm × 1 cm) and dried at 60 °C overnight. Finally, the electrode was pressed under a pressure of 10 MPa. Typically, the loading mass of active material (H-TiO_2/NG) on each current collector was around 3.1 mg, which was acquired by measuring electrode with a microbalance with accuracy of 0.01 mg. Platinum foil (1 cm × 1 cm) and an Ag/AgCl electrode were used as the counter and reference electrode, respectively. The cyclic voltammograms were recorded in a voltage range from −0.05 to +0.5 V at different scanning rates. The cyclic galvanostatic charge/discharge curves were obtained within a potential window of −0.05 to +0.45 V at different current densities. The electrochemical impedance spectroscopy (EIS) was measured at open circuit potential with an Ac perturbation of 5 mV in the frequency range of 100 kHz to 0.01 Hz.

Specific capacitances of single electrode in a three-electrode system were calculated from charge/discharge curves by the following equation:[25]

$$C_s = (I\Delta t)/(m\Delta V) \quad (1)$$

where C_s (F g^{-1}) is specific capacitance of the electrode, I (A) corresponds to the discharge current, ΔV (V) is the potential change within the discharge time Δt (s), and m (g) represents the mass of active material (H-TiO_2/NG).

DOI: 10.1021/acsami.5b04368
ACS Appl. Mater. Interfaces 2015, 7, 17884−17892

Scheme 1. Schematic Illustration of the Formation Process of H-TiO_2/NG Hybrids

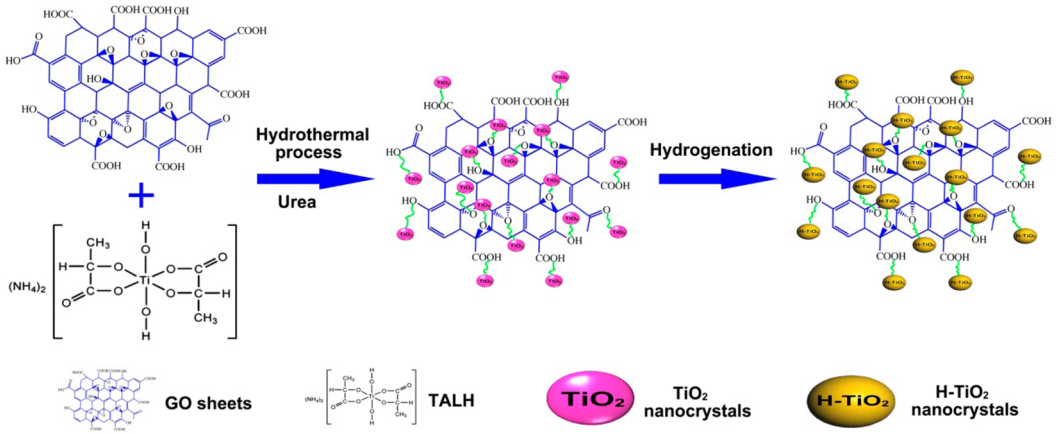

RESULTS AND DISCUSSION

Microstructure Characterizations. The formation process of H-TiO_2/NG hybrids is schematically illustrated in Scheme 1. First, as shown in our previous studies,[27] GO sheets have numerous oxygen-containing groups on their basal planes and edges, which act as anchoring sites for the in situ formation of TiO_2 nanocrystals on the surfaces and edges of GO sheets by hydrothermal process in the presence of urea. Subsequently, the TiO_2 nanocrystals on the surfaces and edges of GO sheets were converted to H-TiO_2 by an annealing in Ar/H_2 (5 wt % H_2) mixed atmosphere.

A general view of H-TiO_2/NG hybrids is shown in Figure 1 and Figure S1 (Supporting Information). It can be seen that H-

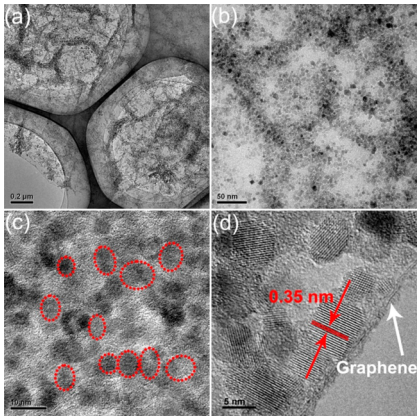

Figure 1. (a) TEM image, (b) zoom-in TEM image, and (c, d) HRTEM images of H-TiO_2/NG-B hybrids.

TiO_2/NG-B presents optimal morphology. Higher amount of H-TiO_2 than 88.7 wt % in hybrids can generate agglomerates of nanoparticles on the surface of graphene. Therefore, the corresponding optimal samples (H-TiO_2/NG-B, TiO_2/NG-B, and H-TiO_2/RGO-B) were selected and discussed below. As shown in Figure 1a,b and Figure S2 (Supporting Information), H-TiO_2 nanocrystals are homogeneously anchored on the surface of graphene sheets. Although the nanocrystals on graphene sheets have a high density, parts of the graphene sheets are still exposed (Figure 1a,b), which is critical for maintaining good contact between individual graphene sheets for high electrical conductivity.[28] In the course of hydrothermal reaction, oxygen-containing functional groups on graphene acting as the heterogeneous nucleation sites can anchor TiO_2 nanocrystals on dispersed active sites so that the agglomeration of these ultrafine nanocrystals can be avoided.[29] Transmission electron microscopy (TEM) studies demonstrate that there are no obvious morphological changes for TiO_2 nanocrystals after annealing under hydrogen atmosphere and the dispersion of the nanocrystals on the graphene sheet is well preserved, while the TiO_2 nanocrystals in situ transform to H-TiO_2 nanocrystals (Figure S3 in the Supporting Information). This result confirms that as-prepared TiO_2 nanocrystals on graphene sheets are stable during high temperature hydrogenation. As evidenced from the high-magnification TEM image (Figure 1c), the ultrafine H-TiO_2 nanocrystals have typical size of 5−10 nm (as indicated by circles in Figure 1c). Such ultrafine nanocrystals are supposed to have more active exposed faces for electrochemical reactions.[26] The high-resolution transmission electron microscopy (HRTEM) image (Figure 1d) shows highly crystalline TiO_2 nanoparticles with an interlayer distance of 0.35 nm, which is in accordance with the (101) plane of anatase phase TiO_2. Moreover, the edge of graphene can be clearly observed as indicated by the arrow (Figure 1d and Figure S4 in the Supporting Information). Compared with multilayered graphene, the few-layer graphene with less agglomeration should be expected to exhibit higher effective surface area and thus better supercapacitor performance.[30] It is worth noting that the H-TiO_2 nanocrystals are still strongly connected with NG sheets even after long time sonication, suggesting a strong interaction between H-TiO_2 nanocrystals and NG sheets, which enables rapid electron transport through the underlying NG sheets to H-TiO_2 nanocrystals, and then results in superior rate capability.

Figure 2a shows the typical X-ray diffraction (XRD) pattern of the H-TiO_2/NG-B, RGO, and NG. For H-TiO_2/NG-B, all of the peaks can be indexed as the tetragonal anatase phase (JCPDS 21−1272). No obvious diffraction peaks for carbon species were observed, indicating that highly disordered and few-layer graphene sheets are in the H-TiO_2/NG-B hybrids because the H-TiO_2 nanocrystals on graphene sheets effectively prevent the graphene sheets from restacking and agglomeration. This is also consistent with the result from TEM images. Raman spectroscopy was employed to analyze the local structure of the H-TiO_2/NG-B hybrids. As observed in Figure 2b, the Raman spectrum of NG shows the typical G-band at 1349 cm^{-1} and D-band at 1575.5 cm^{-1}.[26] The G-band originates from the Raman-active E_{2g} mode, whereas the D-

DOI: 10.1021/acsami.5b04368
ACS Appl. Mater. Interfaces 2015, 7, 17884−17892

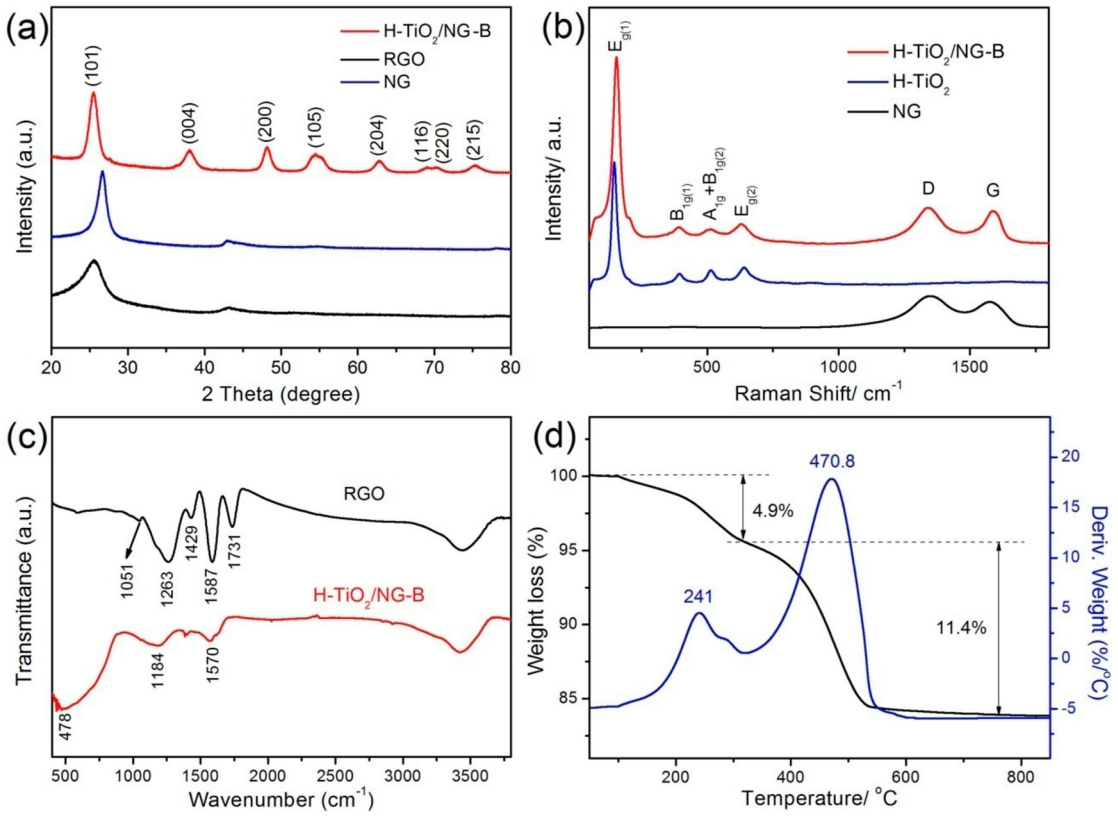

Figure 2. (a) XRD patterns of the H-TiO_2/NG-B, RGO, and NG, (b) Raman spectra of H-TiO_2/NG-B hybrids, H-TiO_2, and NG, (c) Fourier transform infrared spectra of H-TiO_2/NG-B hybrids and RGO, and (d) TGA and DTG curves of TiO_2/NG-B hybrids.

band is associated with disordered graphene.[20] The G-band and D-band in as-synthesized H-TiO_2/NG-B hybrids are similar to those of NG, whereas the four bands located at around 154 ($E_{g(1)}$), 392 ($B_{1g(1)}$), 513 (A_{1g} + $B_{1g(2)}$), and 628 cm^{-1} ($E_{g(2)}$) are characteristic for typical anatase TiO_2 (Figure 2b).[31] The results confirm that NG sheets are decorated with the H-TiO_2 nanocrystals. In addition, a higher intensity ratio of the D band to G band was found in NG (I_D/I_G = 1.04) and H-TiO_2/NG-B (I_D/I_G = 1.11) compared with graphene (I_D/I_G = 0.66) prepared by hydrothermal reduction of GO by our group,[25] indicating a high concentration of structure defects exist on the surface of graphene. It has been well established that the defects of graphene can provide abundant active sites for more electrons storage, which can greatly enhance the capacity of the composites for supercapacitors.[24,25] The active peak for the $E_{g(1)}$ mode of anatase shifts toward high frequency (from 146 cm^{-1} for H-TiO_2 to 154 cm^{-1} for H-TiO_2/NG-B), which is attributed to the electronic interactions between H-TiO_2 and NG.[29] Strong interaction may facilitate fast electron transportation between H-TiO_2 and NG, quicken diffusion kinetics, and thus improve the rate capability. Fourier transform infrared (FTIR) spectroscopy further corroborated the covalent chemical bond between H-TiO_2 and NG (Figure 2c). The FTIR spectrum of reduced graphene oxide (RGO) obtained by hydrothermal reduction clearly showed the characteristic peaks for C═O stretching vibration of the residual COOH groups (1731 cm^{-1}), O−H deformation vibration (1429 cm^{-1}), C−O vibration of the carboxy (1263 cm^{-1}), and C−O−C vibration of the epoxy (1051 cm^{-1}), respectively.[27] For H-TiO_2/NG-B, the broad absorption at low frequency (400−900 cm^{-1}) was much plumper than the corresponding peak in H-TiO_2 and shifted toward high wavenumber (from 466 to 478 cm^{-1}), which was attributed to a combination of Ti−O−Ti vibration and Ti−O−C vibration (Figure S5a in the Supporting Information).[32−34] Besides, no peaks relating to the C═O, O−H, C−OH, and C−O−C groups could be observed, while the absorption band (ca. 1570 cm^{-1}) for the graphene sheets still retain, also indicating the epoxy C−O and hydroxyl O−H groups have been broken down to form a Ti−O−C covalent bond between graphene and TiO_2 nanocrystals. Moreover, a broad peak at 1184 cm^{-1} for N−C bonds appeared, indicating the formation of NG during the hydrothermal reaction.[35] The amount of TiO_2 in TiO_2/NG-B hybrids was determined by thermal-gravimetric measurements. Based on the differential thermogravimetric (DTG) curve in Figure 2d, the weight loss in the temperature range of 50−200 °C was due to the removal of the adsorbed water and the residual oxygen groups on the surface of graphene, whereas the weight loss at about 470.8 °C was attributed to the burning of the carbon skeleton of graphene.[27,36] According to thermogravimetric analysis (TGA) in Figure 2d, the TiO_2 accounts for 88.6 wt % in the TiO_2/NG-B hybrids, which agrees with the theoretical proportion of TiO_2 (91.1 wt %) resulting from experimental design. This results indicate that the TiO_2 nanocrystals anchored on the surface of graphene sheets through in situ growth.[37] In addition, the content of H-TiO_2 in the H-TiO_2/NG-B hybrids and H-TiO_2/RGO-B hybrids was also determined by thermal-gravimetric measurements (Figure S5b in the Supporting Information). It can be seen that the H-TiO_2 contents in the H-TiO_2/NG-B hybrids (88.7 wt %) and H-TiO_2/RGO-B hybrids (88.5 wt %) are almost same, which is also in accord with the TiO_2 contents in the TiO_2/NG-B hybrids (88.6 wt %).

To investigate the composition and the chemical bonding environment in the H-TiO_2/NG-B hybrids, the X-ray photo-

DOI: 10.1021/acsami.5b04368
ACS Appl. Mater. Interfaces 2015, 7, 17884−17892

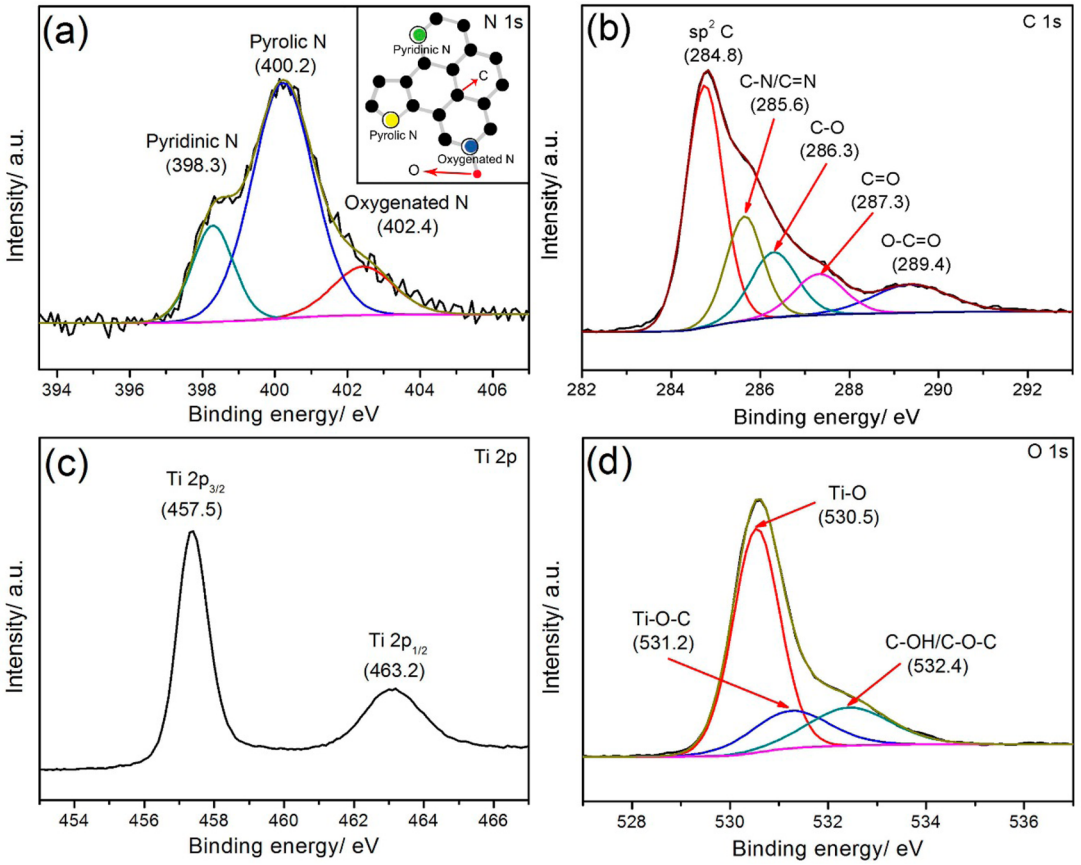

Figure 3. (a) Narrow spectra of N 1s (the inset shows the nitrogen bonding configurations in NG), (b) the narrow spectra of C 1s, (c) the narrow spectra of Ti 2p, and (d) the narrow spectra of O 1s for H-TiO_2/NG-B hybrids.

electron spectroscopy (XPS) measurements were carried out. The XPS revealed the presence of the principal C, Ti, O, and N elements, and 2.39 at. % nitrogen in H-TiO_2/NG-B hybrids (Figure S6a in the Supporting Information), but no N element was detected in the H-TiO_2/RGO-B sample made without urea (Figure S6b in the Supporting Information). High resolution XPS spectra of the N peak revealed pyridinic N (398.3 eV), pyrolic N (400.2 eV), and oxygenated N (402.4 eV) species in H-TiO_2/NG-B hybrids (Figure 3a). The nitrogen bonding configurations within the graphene are illustrated in the inset of Figure 3a. The pyrolic N and the pyridinic N play a crucial role in improving the electrochemical properties of graphene, which has been demonstrated in our previous study.[25,26] For the high resolution C 1s peak, the main peak centered at about 284.8 eV originated from the graphitic sp^2 carbon atoms, whereas the binding energies located at 286.3, 287.3, and 289.4 eV were attributed to epoxy (C−O), carbonyl (C═O), and carboxylate (O−C═O) groups.[38,39] Moreover, an additional component centered at 285.6 eV due to the carbon bound to nitrogen (C−N/C═N) was observed, which verified that N was successfully doped into the graphene.[35,36] In the spectra of Ti 2p (Figure 4c), two broad peaks centered at 457.5 and 463.2 eV correspond to the characteristic Ti $2p_{3/2}$ and Ti $2p_{1/2}$ peaks, which are typical of Ti^{3+} in an octahedral environment,[7] indicating the oxygen vacancies exist in H-TiO_2 nanocrystals. This result confirms the as-prepared TiO_2 nanocrystals are hydrogenated TiO_2. However, the characteristic peak (396 eV) of the Ti−N−Ti linkages could not be observed, suggesting that the nitrogen atoms did not dope into the TiO_2 lattice.[40] The high resolution O 1s spectrum exhibited that the intensity of peaks related to oxygenated groups in the H-TiO_2/NG-B hybrids was much lower than those of RGO gained from hydrothermal reduction, suggesting a reaction between oxygenated groups and TiO_2 nanocrystals during the hydrothermal process (Figure S7 in the Supporting Information). Moreover, the peak at around 531.2 eV is assigned to O in Ti−O−C covalent bond, while that at approximately 530.5 eV is assigned to the bulk oxygen (O^{2-}) in TiO_2.[41,42] These results further confirm the strong interaction between TiO_2 and graphene through the formation of Ti−O−C covalent bond, which is in agreement with the FTIR results.

Electrochemical Behaviors. The electrochemical properties of the H-TiO_2/NG-B hybrids were evaluated in a three-electrode electrochemical cell with a platinum foil (1 cm × 1 cm) counter electrode and an Ag/AgCl reference electrode in 1 M KOH aqueous solution. Figure 4a shows the cyclic voltammograms (CV) of the H-TiO_2/NG-B electrode collected at the scan rates of 5, 10, 20, 50, and 100 mV/s with potential windows ranging from 0 to 0.5 V. All the CV curves exhibit a pair of cathodic and anodic peaks, which indicates the capacitance is mainly from the Faradaic mechanism neglecting the capacitance of the nickel foam substrate (Figure S8a in the Supporting Information). Similar to the charge storage mechanism of the previous report,[6] the redox peaks of the H-TiO_2/NG-B hybrids are attributed to the surface or subsurface intercalation and deintercalation cation processes according to

$$(TiO_2)_{surface} + M^+ + e^- \leftrightarrow (TiO_2^-M^+)_{surface} \quad (2)$$

where M can be H_3O^+ or K^+ in the electrolyte.

DOI: 10.1021/acsami.5b04368
ACS Appl. Mater. Interfaces 2015, 7, 17884−17892

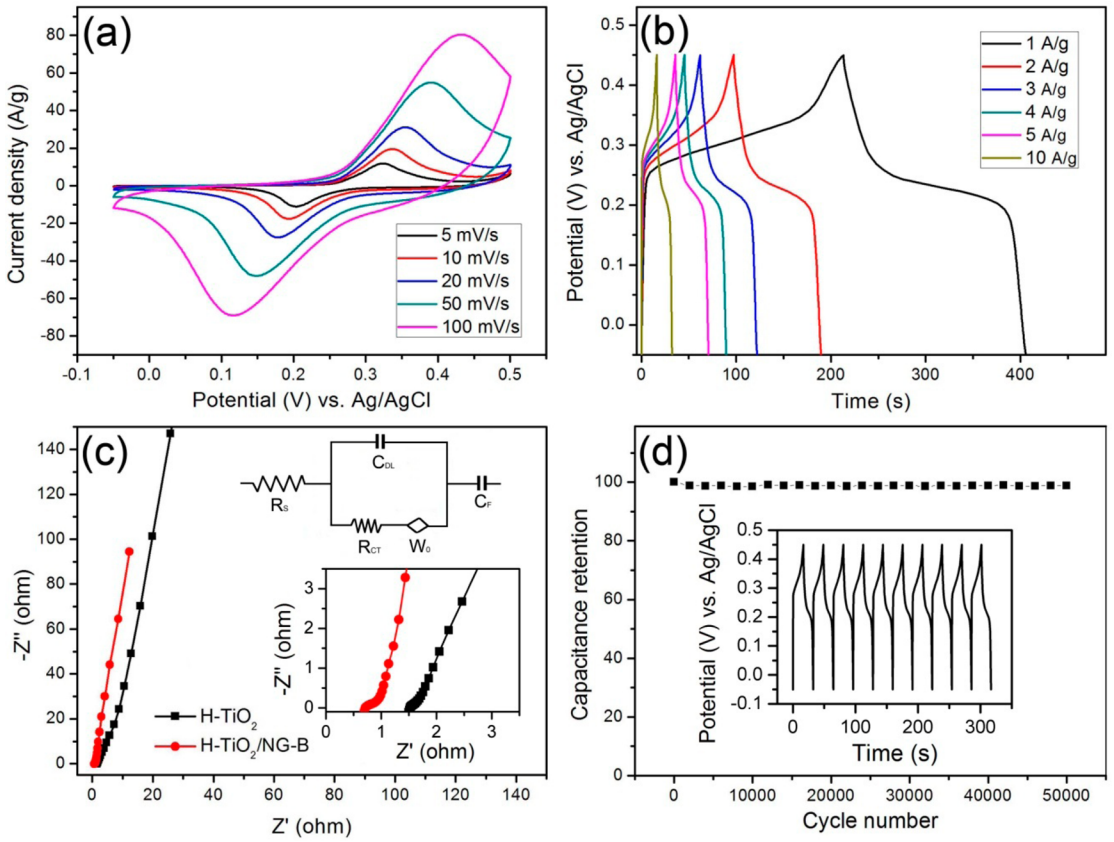

Figure 4. (a) CV curves of the H-TiO_2/NG-B hybrids at different scan rates, (b) CD curves of the H-TiO_2/NG-B hybrids at various current densities, (c) EIS of the H-TiO_2/NG-B hybrids and H-TiO_2 nanocrystals (the insets show the enlarged EIS at the high frequency region (bottom) and the electrical equivalent circuit used for fitting impedance spectra (top)), and (d) cycle life of the H-TiO_2/NG-B hybrids at 10 A g^{-1} by a three-electrode configuration in 1 M KOH aqueous solution.

Over the entire range of scan rates, the pair of redox peaks is nearly symmetrical, revealing good reversibility of the redox reactions in the H-TiO_2/NG-B electrode.[11] When the scan rate increases, the oxidation peaks shifted to a more positive position and the reduction peaks to a more negative position, which results from an increase of the internal diffusion resistance in the pseudoactive material. But, the peak current intensity increases linearly with the scan rate, confirming the excellent kinetics of interfacial faradic redox reactions and the rapid rates of electronic and ionic transport in the H-TiO_2/NG-B electrode (Figure S8b in the Supporting Information).[11] Figure 4b presents the typical galvanostatic charge/discharge (CD) curves of H-TiO_2/NG-B electrode at different current densities within a potential range of −0.05 to +0.45 V. Clearly, the discharge curves exhibit two sections, a sudden potential drop and a slow potential decay. The first potential drop is mainly due to the internal resistance, and the subsequent potential decay represents the capacitive characteristics of the electrode. The obvious deviation of the shape of the discharge curves from the straight lines indicates the Faradaic characteristics of the charge storage, consistent with the CV results. The capacitance of the H-TiO_2/NG-B calculated from CD curves at a current density of 1 A g^{-1} is 385.2 F g^{-1}. Even at a high current density of 10 A g^{-1}, it still delivers a capacitance of 320.1 F g^{-1}, indicating excellent rate capability (Figure S9a in the Supporting Information). This result indicates a much improved capacity of the H-TiO_2/NG-B hybrids compared with previous studies for TiO_2-based electrode, such as graphene/ALD TiO_2 electrode (84 F/g),[6] carbon/mesoporous TiO_2(18.4 F/g),[15] carbon nanotubes/TiO_2 nanoparticles (180 F/g).[16] In comparison with NG, pure H-TiO_2, H-TiO_2/NG-A, and H-TiO_2/NG-C electrode, the H-TiO_2/NG-B electrode delivers significantly higher specific capacitance, indicating a strong synergistic effect and optimum ratio between NG sheets and H-TiO_2 nanocrystals achieved (Figure S9b in the Supporting Information). The NG sheets provide an excellent conductivity and more active sites, whereas the ultrafine H-TiO_2 nanocrystals with uniform dispersions can be substantially utilized during the electrochemical process. Thus, the H-TiO_2/NG-B with well-defined nanostructure can accelerate the electron transport and facilitate the redox reactions in the whole electrode, significantly enhancing the kinetic requirements for an ideal electrode material. The electrochemical performance of the H-TiO_2/NG-B electrode was further investigated by using electrochemical impedance spectroscopy (EIS) (Figure 4c). The measured impedance spectra were analyzed using the complex nonlinear least-squares (CNLS) fitting method on the basis of the equivalent circuit (Figure 4c), where R_S is solution resistance, C_{DL} is double-layer capacitance, W_o is the finite-length Warburg diffusion element, R_{CT} is charge-transfer resistance, and C_F is the faradic capacitance. The impedance spectra can be classified into two regions, including a semicircle at the higher frequency region and a straight line at the lower frequency region. At high frequency, the intercept at the real axis represents the equivalent series resistance (ESR), which is due to electric resistance of the electrode materials and interface resistance. Compared with H-TiO_2 electrode (1.52 Ω), the H-TiO_2/NG-B electrode displays a lower equivalent

DOI: 10.1021/acsami.5b04368
ACS Appl. Mater. Interfaces 2015, 7, 17884−17892

series resistance (0.71 Ω), indicating an improved conductivity for H-TiO_2/NG-B electrode due to the incorporation of NG. In the lower frequency area, the straight line was determined by ion diffusion. For the H-TiO_2 electrode and the H-TiO_2/NG-B electrode, the slope of the straight line associated with H-TiO_2/NG-B electrode was larger than H-TiO_2 electrode and closer to the imaginary impedance axis (Z″), which shows a lower diffusion resistance and an ideal polarizable capacitance. As discussed above, we might conclude that the combination of low equivalent series resistance and diffusion resistance is responsible for the excellent electrochemical performance of the hybrid structure. Figure 4d reveals the cycle performance of the H-TiO_2/NG-B electrode measured at a high current density of 10 A g^{-1} for 50 000 cycles. The H-TiO_2/NG-B still retains 98.8% of its initial capacitance after 50 000 cycles, demonstrating excellent stable cycling performance and a high level of reversibility of H-TiO_2/NG-B hybrids. Such performance is much better than TiO_2-based electrode reported previously,[6,17,18] which can be attributed to the enhanced electric conductivity and electrochemical activity of ultrafine H-TiO_2 nanocrystals by introducing oxygen vacancies (Ti^{3+} sites) in TiO_2 lattices, the excellent electronic highway and mechanical backbone provided by NG matrices, and the strong interaction between TiO_2 nanocrystals and NG sheets via covalent chemical bonding.

To further demonstrate the remarkable capacitive properties of H-TiO_2/NG-B hybrids for supercapacitors, the CV and CD measurements of H-TiO_2/RGO-B hybrids and TiO_2/NG-B hybrids were also carried out under the same test conditions for comparison. Figure 5a shows the CV curves of the H-TiO_2/NG-B, H-TiO_2/RGO-B, and TiO_2/NG-B electrodes obtained at the scan rate of 50 mV s^{-1}. It can be seen that the voltammetric currents and curve areas of the H-TiO_2/NG-B are much higher than those of H-TiO_2/RGO-B and TiO_2/NG-B at the same scan rate. This clearly confirms that the H-TiO_2/NG-B electrodes are superlative among three pseudocapacitive electrodes. Furthermore, the larger separation between leveled anodic and cathodic currents at the same scan rates for the H-TiO_2/NG-B electrode further confirmes its larger specific capacitances. Figure 5b shows the CD curves of the H-TiO_2/NG-B, H-TiO_2/RGO-B, and TiO_2/NG-B electrodes at a current density of 1 A g^{-1}. As expected, the H-TiO_2/NG-B hybrid electrode shows the longer charge−discharge time compared to those of H-TiO_2/RGO-B, and TiO_2/NG-B electrodes. The specific capacitance of H-TiO_2/NG-B, H-TiO_2/RGO-B, and TiO_2/NG-B calculated from the CD curves at 1 A g^{-1} are 385.2, 62.8, and 110.5 F g^{-1}, respectively. Consistent with the CV results, the specific capacitance of H-TiO_2/NG-B electrodes was much higher than those of H-TiO_2/RGO-B and TiO_2/NG-B electrodes, which also demonstrates the excellent synergistic effect of the H-TiO_2/NG-B hybrid electrode. To further understand the electrochemical performance characteristics, the EIS was carried out (Figure 5c). In comparison to the H-TiO_2/RGO-B and TiO_2/NG-B electrodes, H-TiO_2/NG-B electrode shows a much smaller equivalent series resistance in the Nyquist plots, which can be attributed to the higher electric conductivity of H-TiO_2/NG-B electrode due to strong synergistic effect and covalent interactions between H-TiO_2 nanocrystals and NG sheets.[43] The results clearly confirm that the H-TiO_2/NG-B has favorable charge-transfer kinetics as an electrode for supercapacitors and thus shows an enhanced pseudocapacitive performance. Cycling stability is another important parameter for supercapacitor applications of the electrode materials. The H-TiO_2/NG-B, H-TiO_2/RGO-B, and TiO_2/NG-B electrodes were invesitgated at a current density of 10 A g^{-1} for 50 000 cycles, as shown in Figure 5d. It can be observed that the capacitance retention of H-TiO_2/NG-B electrode is 98.8%, whereas the capacitance retentions of H-TiO_2/RGO-B and TiO_2/NG-B electrodes are 74.5% and 81.7%, respectively, after 50 000 cycles. This can be mainly attributed to the significantly improved ion diffusion and electron transport rate and decreased ohmic resistance for the H-TiO_2/NG-B sample after the hydrogenation of TiO_2 nanocrystals and the nitrogen doping of graphene. Clearly, all these results prove that H-TiO_2/NG-B electrode exhibits excellent electrochemical properties for supercapacitors.

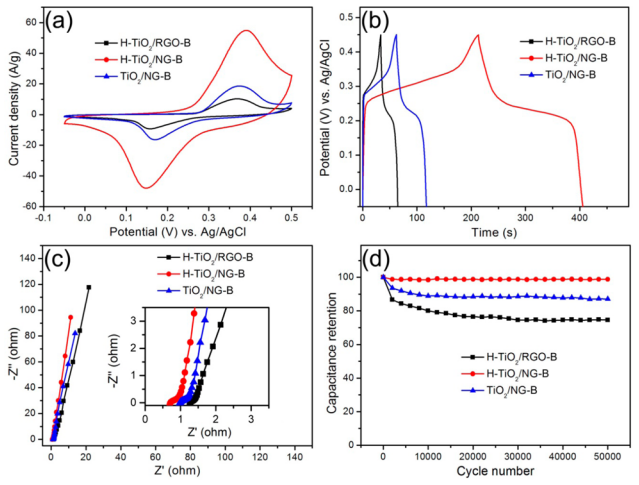

Figure 5. (a) CV curves for the H-TiO_2/NG-B, H-TiO_2/RGO-B, and TiO_2/NG-B electrodes collected at the scan rate of 50 mV s^{-1}, (b) CD curves for the H-TiO_2/NG-B, H-TiO_2/RGO-B, and TiO_2/NG-B electrodes at a current density of 1 A g^{-1}, (c) EIS for the H-TiO_2/NG-B, H-TiO_2/RGO-B, and TiO_2/NG-B electrodes (the inset shows the enlarged EIS at the high frequency region), and (d) cycle performance for the H-TiO_2/NG-B, H-TiO_2/RGO-B, and TiO_2/NG-B electrodes at a current density of 10 A g^{-1} for 50 000 cycles.

CONCLUSIONS

In summary, the hydrogenated TiO_2 nanocrystals/nitrogen-doped graphene (H-TiO_2/NG) hybrids were developed by a simple and effective route. It was demonstrated that the optimized H-TiO_2/NG (H-TiO_2/NG-B) electrodes exhibit high specific capacity of 385.2 F g^{-1} at 1 A g^{-1}, rapid charge/discharge kinetics, and excellent long-term stability with capacitance retention of 98.8% after 50 000 cycles. The enhanced electrochemical performance can be attributed to the improved electric conductivity and electrochemical activity of H-TiO_2 nanocrystals by introducing oxygen vacancies (Ti^{3+} sites) in TiO_2 lattices and the superior electronic highway and mechanical scaffold provided by the NG network. Furthermore, the strong interaction between TiO_2 nanocrystals and NG sheets via covalent chemical bonding can afford high structural stability, thus inhibiting the aggregation of H-TiO_2 and maintaining the structural integrity. The finding gained from this study should be valuable in the development of high-performance electrode materials for supercapacitors.

DOI: 10.1021/acsami.5b04368
ACS Appl. Mater. Interfaces 2015, 7, 17884−17892

■ ASSOCIATED CONTENT

Supporting Information

The Supporting Information is available free of charge on the ACS Publications website at DOI: 10.1021/acsami.5b04368.

Additional figures (Figures S1−S9) of TEM, SEM, HRTEM, FTIR, and XPS spectra; CV curves; and CD curves (PDF)

■ AUTHOR INFORMATION

Corresponding Authors

*Tel: +86-21-52412718. Fax: +86-21-52413122. E-mail: songxfeng@sjtu.edu.cn (X.S.).

*E-mail: liangao@mail.sic.ac.cn (L.G.).

Notes

The authors declare no competing financial interest.

■ ACKNOWLEDGMENTS

The authors greatly acknowledge the financial support by the National Natural Science Foundation of China (51302169 and 51172142), the SJTU-SMC Foundation for Excellent Young Teacher, the Shanghai Aerospace Science and Technology Innovation Foundation Project, and the Third Phase of 211 Project for Advanced Materials Science (WS3116205007).

■ REFERENCES

(1) Jiang, J.; Li, Y.; Liu, J.; Huang, X.; Yuan, C.; Lou, X. W. D. Recent Advances in Metal Oxide-Based Electrode Architecture Design for Electrochemical Energy Storage. *Adv. Mater.* **2012**, *24*, 5166−5180.

(2) Yan, J.; Wang, Q.; Wei, T.; Fan, Z. Recent Advances in Design and Fabrication of Electrochemical Supercapacitors with High Energy Densities. *Adv. Energy Mater.* **2014**, *4*, 1−43.

(3) Xu, C.; Xu, B.; Gu, Y.; Xiong, Z.; Sun, J.; Zhao, X. Graphene-Based Electrodes for Electrochemical Energy Storage. *Energy Environ. Sci.* **2013**, *6*, 1388−1414.

(4) Liu, F.; Song, S.; Xue, D.; Zhang, H. Folded Structured Graphene Paper for High Performance Electrode Materials. *Adv. Mater.* **2012**, *24*, 1089−1094.

(5) Wang, R.; Yan, X.; Lang, J.; Zheng, Z.; Zhang, P. A Hybrid Supercapacitor Based on Flower-Like $Co(OH)_2$ and Urchin-Like VN Electrode Materials. *J. Mater. Chem. A* **2014**, *2*, 12724−12732.

(6) Sun, X.; Xie, M.; Wang, G.; Sun, H.; Cavanagh, A. S.; Travis, J. J.; George, S. M.; Lian, J. Atomic Layer Deposition of TiO_2 on Graphene for Supercapacitors. *J. Electrochem. Soc.* **2012**, *159*, A364−A369.

(7) Lu, X.; Wang, G.; Zhai, T.; Yu, M.; Gan, J.; Tong, Y.; Li, Y. Hydrogenated TiO_2 Nanotube Arrays for Supercapacitors. *Nano Lett.* **2012**, *12*, 1690−1696.

(8) Wu, H.; Xu, C.; Xu, J.; Lu, L.; Fan, Z.; Chen, X.; Song, Y.; Li, D. Enhanced Supercapacitance in Anodic TiO_2 Nanotube Films by Hydrogen Plasma Treatment. *Nanotechnology* **2013**, *24*, 455401.

(9) Liu, H. K. Enhancement of the Capacitance in TiO_2 Nanotubes through Controlled Introduction of Oxygen Vacancies. *J. Mater. Chem.* **2011**, *21*, 5128−5133.

(10) Salari, M.; Aboutalebi, S. H.; Konstantinov, K.; Liu, H. K. A Highly Ordered Titania Nanotube Array as a Supercapacitor Electrode. *Phys. Chem. Chem. Phys.* **2011**, *13*, 5038−5041.

(11) Kim, J. H.; Zhu, K.; Yan, Y.; Perkins, C. L.; Frank, A. J. Microstructure and Pseudocapacitive Properties of Electrodes Constructed of Oriented NiO-TiO_2 Nanotube Arrays. *Nano Lett.* **2010**, *10*, 4099−4104.

(12) Xu, C.; Song, Y.; Lu, L.; Cheng, C.; Liu, D.; Fang, X.; Chen, X.; Zhu, X.; Li, D. Electrochemically Hydrogenated TiO_2 Nanotubes with Improved Photoelectrochemical Water Splitting Performance. *Nanoscale Res. Lett.* **2013**, *8*, 391.

(13) Wu, H.; Li, D.; Zhu, X.; Yang, C.; Liu, D.; Chen, X.; Song, Y.; Lu, L. High-Performance and Renewable Supercapacitors Based on TiO_2 Nanotube Array Electrodes Treated by an Electrochemical Doping Approach. *Electrochim. Acta* **2014**, *116*, 129−136.

(14) Wang, Q.; Wen, Z.; Li, J. Carbon Nanotubes/TiO_2 Nanotubes Hybrid Supercapacitor. *J. Nanosci. Nanotechnol.* **2007**, *7*, 3328−3331.

(15) Lu, L.; Zhu, Y.; Li, F.; Zhuang, W.; Chan, K. Y.; Lu, X. Carbon Titania Mesoporous Composite Whisker as Stable Supercapacitor Electrode Material. *J. Mater. Chem.* **2010**, *20*, 7645−7651.

(16) Hsieh, C. T.; Chang, C. C.; Chen, W. Y.; Hung, W. M. Electrochemical Capacitance from Carbon Nanotubes Decorated with Titanium Dioxide Nanoparticles in Acid Electrolyte. *J. Phys. Chem. Solids* **2009**, *70*, 916−921.

(17) Ramadoss, A.; Kim, S. J. Improved Activity of a Graphene-TiO_2 Hybrid Electrode in an Electrochemical Supercapacitor. *Carbon* **2013**, *63*, 434−445.

(18) Xiang, C.; Li, M.; Zhi, M.; Manivannan, A.; Wu, N. Reduced Graphene Oxide/Titanium Dioxide Composites for Supercapacitor Electrodes: Shape and Coupling Effects. *J. Mater. Chem.* **2012**, *22*, 19161−19167.

(19) Lu, X.; Yu, M.; Wang, G.; Zhai, T.; Xie, S.; Ling, Y.; Tong, Y.; Li, Y. H-TiO_2@MnO_2//H-TiO_2@C Core-Shell Nanowires for High Performance and Flexible Asymmetric Supercapacitors. *Adv. Mater.* **2013**, *25*, 267−272.

(20) Wang, H.; Maiyalagan, T.; Wang, X. Review on Recent Progress in Nitrogen-Doped Graphene: Synthesis, Characterization, and Its Potential Applications. *ACS Catal.* **2012**, *2*, 781−794.

(21) Han, J.; Zhang, L. L.; Lee, S.; Oh, J.; Lee, K. S.; Potts, J. R.; Ji, J.; Zhao, X.; Ruoff, R. S.; Park, S. Generation of B-Doped Graphene Nanoplatelets Using a Solution Process and Their Supercapacitor Applications. *ACS Nano* **2013**, *7*, 19−26.

(22) Wen, Z.; Wang, X.; Mao, S.; Bo, Z.; Kim, H.; Cui, S.; Lu, G.; Feng, X.; Chen, J. Crumpled Nitrogen-Doped Graphene Nanosheets with Ultrahigh Pore Volume for High-Performance Supercapacitor. *Adv. Mater.* **2012**, *24*, 5610−5616.

(23) You, B.; Wang, L.; Yao, L.; Yang, J. Three Dimensional N-Doped Graphene-CNT Networks for Supercapacitor. *Chem. Commun.* **2013**, *49*, 5016−5018.

(24) Jeong, H. M.; Lee, J. W.; Shin, W. H.; Choi, Y. J.; Shin, H. J.; Kang, J. K.; Choi, J. W. Nitrogen-Doped Graphene for High-Performance Ultracapacitors and the Importance of Nitrogen-Doped Sites at Basal Planes. *Nano Lett.* **2011**, *11*, 2472−2477.

(25) Yang, S.; Song, X.; Zhang, P.; Gao, L. Facile Synthesis of Nitrogen-Doped Graphene-Ultrathin MnO_2 Sheet Composites and Their Electrochemical Performances. *ACS Appl. Mater. Interfaces* **2013**, *5*, 3317−3322.

(26) Yang, S.; Song, X.; Zhang, P.; Gao, L. Crumpled Nitrogen-Doped Graphene-Ultrafine Mn_3O_4 Nanohybrids and Their Application in Supercapacitors. *J. Mater. Chem. A* **2013**, *1*, 14162−14169.

(27) Yang, S.; Song, X.; Zhang, P.; Sun, J.; Gao, L. Self-Assembled α-Fe_2O_3 Mesocrystals/Graphene Nanohybrid for Enhanced Electrochemical Capacitors. *Small* **2014**, *10*, 2270−2279.

(28) Etacheri, V.; Yourey, J. E.; Bartlett, B. M. Chemically Bonded TiO_2-Bronze Nanosheet/Reduced Graphene Oxide Hybrid for High-Power Lithium Ion Batteries. *ACS Nano* **2014**, *8*, 1491−1499.

(29) Li, N.; Liu, G.; Zhen, C.; Li, F.; Zhang, L.; Cheng, H. M. Battery Performance and Photocatalytic Activity of Mesoporous Anatase TiO_2 Nanospheres/Graphene Composites by Template-Free Self-Assembly. *Adv. Funct. Mater.* **2011**, *21*, 1717−1722.

(30) Wang, Y.; Shi, Z.; Huang, Y.; Ma, Y.; Wang, C.; Chen, M.; Chen, Y. Supercapacitor Devices Based on Graphene Materials. *J. Phys. Chem. C* **2009**, *113*, 13103−13107.

(31) Huang, Q.; Tian, S.; Zeng, D.; Wang, X.; Song, W.; Li, Y.; Xiao, W.; Xie, C. Enhanced Photocatalytic Activity of Chemically Bonded TiO_2/Graphene Composites Based on the Effective Interfacial Charge Transfer through the C-Ti Bond. *ACS Catal.* **2013**, *3*, 1477−1485.

(32) Sakthivel, S.; Kisch, H. Daylight Photocatalysis by Carbon-Modified Titanium Dioxide. *Angew. Chem., Int. Ed.* **2003**, *42*, 4908−4911.

(33) Zhang, H.; Lv, X.; Li, Y.; Wang, Y.; Li, J. P25-Graphene Composite as a High Performance Photocatalyst. *ACS Nano* **2010**, *4*, 380−386.
(34) Sun, L.; Zhao, Z.; Zhou, Y.; Liu, L. Anatase TiO_2 Nanocrystals with Exposed {001} Facets on Graphene Sheets Via Molecular Grafting for Enhanced Photocatalytic Activity. *Nanoscale* **2012**, *4*, 613−620.
(35) Lin, Z.; Waller, G.; Liu, Y.; Liu, M.; Wong, C. P. Facile Synthesis of Nitrogen-Doped Graphene Via Pyrolysis of Graphene Oxide and Urea, and Its Electrocatalytic Activity toward the Oxygen-Reduction Reaction. *Adv. Energy Mater.* **2012**, *2*, 884−888.
(36) Zhang, J.; Jiang, J.; Zhao, X. Synthesis and Capacitive Properties of Manganese Oxide Nanosheets Dispersed on Functionalized Graphene Sheets. *J. Phys. Chem. C* **2011**, *115*, 6448−6454.
(37) Qiu, B.; Xing, M.; Zhang, J. Mesoporous TiO_2 Nanocrystals Grown in Situ on Graphene Aerogels for High Photocatalysis and Lithium-Ion Batteries. *J. Am. Chem. Soc.* **2014**, *136*, 5852−5855.
(38) Akhavan, O.; Ghaderi, E.; Rahimi, K. Adverse Effects of Graphene Incorporated in TiO_2 Photocatalyst on Minuscule Animals under Solar Light Irradiation. *J. Mater. Chem.* **2012**, *22*, 23260−23266.
(39) Sasidharan, A.; Panchakarla, L.; Chandran, P.; Menon, D.; Nair, S.; Rao, C.; Koyakutty, M. Differential Nano-Bio Interactions and Toxicity Effects of Pristine Versus Functionalized Graphene. *Nanoscale* **2011**, *3*, 2461−2464.
(40) Jiang, X.; Yang, X.; Zhu, Y.; Jiang, H.; Yao, Y.; Zhao, P.; Li, C. 3D Nitrogen-Doped Graphene Foams Embedded with Ultrafine TiO_2 Nanoparticles for High-Performance Lithium-Ion Batteries. *J. Mater. Chem. A* **2014**, *2*, 11124−11133.
(41) Li, G.; Li, L.; Boerio-Goates, J.; Woodfield, B. F. High Purity Anatase TiO_2 Nanocrystals: Near Room-Temperature Synthesis, Grain Growth Kinetics, and Surface Hydration Chemistry. *J. Am. Chem. Soc.* **2005**, *127*, 8659−8666.
(42) Ong, W. J.; Tan, L. L.; Chai, S. P.; Yong, S. T.; Mohamed, A. R. Self-Assembly of Nitrogen-Doped TiO_2 with Exposed {001} Facets on a Graphene Scaffold as Photo-Active Hybrid Nanostructures for Reduction of Carbon Dioxide to Methane. *Nano Res.* **2014**, *7*, 1528−1547.
(43) Xiao, J.; Wan, L.; Yang, S.; Xiao, F.; Wang, S. Design Hierarchical Electrodes with Highly Conductive $NiCo_2S_4$ Nanotube Arrays Grown on Carbon Fiber Paper for High-Performance Pseudocapacitors. *Nano Lett.* **2014**, *14*, 831−838.

DOI: 10.1021/acsami.5b04368
ACS Appl. Mater. Interfaces 2015, 7, 17884−17892